Diurnal Cycle of Thermally Driven Cross-Basin Winds in Arizona's Meteor Crater

MANUELA LEHNER, C. DAVID WHITEMAN, AND SEBASTIAN W. HOCH

University of Utah, Salt Lake City, Utah

(Manuscript received 25 March 2010, in final form 2 November 2010)

ABSTRACT

Cross-basin winds produced by asymmetric insolation of the crater sidewalls occur in Arizona's Meteor Crater on days with weak background winds. The diurnal cycle of the cross-basin winds is analyzed together with radiation, temperature, and pressure measurements at the crater sidewalls for a 1-month period. The asymmetric irradiation causes horizontal temperature and pressure gradients across the crater basin that drive the cross-basin winds near the crater floor. The horizontal temperature and pressure gradients and wind directions change as the sun moves across the sky, with easterly winds in the morning and westerly winds in the evening. A case study of 12 October 2006 further illustrates the obtained relation between these parameters for an individual day. The occurrence of an elevated cross-basin flow on 23 October 2006 is shown to relate to the presence of an elevated inversion layer.

1. Introduction

The well-known conceptual model of Defant (1949) of thermally driven wind systems in valleys describes the phases of the valley and slope wind systems and their relationships. The transitions from downslope to upslope flows in the morning and from upslope to downslope flows in the afternoon are represented in this conceptual model as being symmetric with respect to the valley axis. In most real cases, however, the orientation of the valley sidewalls with respect to the sun forces asymmetric irradiation conditions (Whiteman et al. 1989; Matzinger et al. 2003; Hoch and Whiteman 2010) that cause flow transitions to occur at different times on the opposing sidewalls and lead to cross-valley flows. Let us assume a simple north–south-oriented valley for which the mountain sidewalls face the east and west, respectively (Fig. 1). As the sun rises in the morning, the east-facing slope is illuminated immediately while the west-facing slope is still shaded from direct irradiation. The opposite situation occurs in the evening before sunset. This has two major implications on the slope and valley wind systems. First, upslope winds evolve asymmetrically in the morning according to the times of local sunrise on the respective sidewalls. The effects of this asymmetry on dynamics and air pollution have been noted in both observational (e.g., Gudiksen and Shearer 1989; Orgill 1989; Gohm et al. 2009) and modeling studies (e.g., Segal et al. 1987; Anquetin et al. 1998; Colette et al. 2003; Lehner and Gohm 2010). Second, a horizontal temperature and, thus, pressure gradient develops across the valley, producing a cross-valley wind that is directed toward the sunlit–warmer sidewall. Several studies, most conducted before the late 1980s, dealt with this cross-valley flow (e.g., Moll 1935; MacHattie 1968; Hennemuth 1986; Whiteman 1989; Bader and Whiteman 1989). Urfer-Henneberger (1970) expanded Defant's schematic model to include cross-valley winds that blew toward the sunlit slope, based on observations in Switzerland's Dischma Valley. Gleeson (1951) used an analytical model to estimate cross-valley wind components and compared his results with observations from the Columbia River Valley in Canada. He derived horizontal temperature gradients from theoretical irradiation as a function of the sun's position, valley orientation, and slope angle. Egger (1981) developed a numerical model for thermal wind circulations that also showed cross-valley winds in the presence of asymmetric heating of the valley sidewalls. Hennemuth (1986) provided a short overview of previous work on thermally and dynamically driven cross-valley winds. Hennemuth and Schmidt (1985) showed that cross-valley winds in the Dischma Valley were particularly pronounced during the morning and evening transition periods, when along-valley

Corresponding author address: Manuela Lehner, Dept. of Atmospheric Sciences, University of Utah, 135 S 1460 E, Rm. 819, Salt Lake City, UT 84112-0110.
E-mail: manuela.lehner@utah.edu

DOI: 10.1175/2010JAMC2520.1

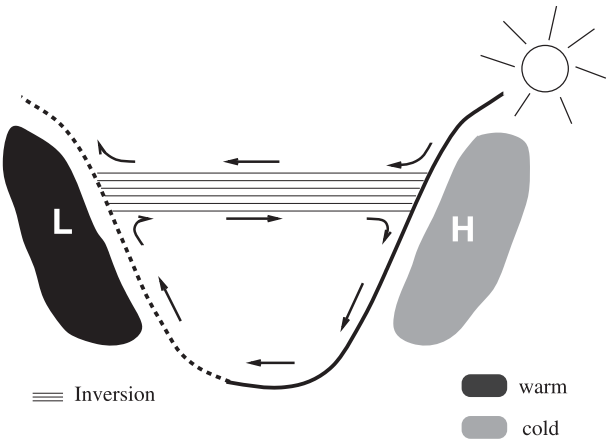

FIG. 1. Cross-valley wind field in the presence of asymmetric insolation. The dashed line indicates the illuminated valley sidewall, while the solid line indicates the shaded sidewall. The letters L and H denote areas of low and high pressure, respectively.

winds were weak, even though the maximum in irradiation difference occurred during the day. During the day, however, the cross-valley wind component led to a deflection of the valley wind. Perhaps it is because cross-valley winds are comparatively weak and are often overlaid by stronger along-valley winds that cross-valley winds have received little research attention since the 1980s.

In this paper we present observations of cross-basin flows in Arizona's Meteor Crater. We investigate the interrelationship between asymmetric irradiation of the crater sidewalls and the development of horizontal temperature and pressure gradients, and cross-basin flows in the crater basin. For this purpose, mean diurnal cycles of cross-basin winds and horizontal differences of slope-parallel global radiation, temperature, and pressure between opposite crater sidewalls are analyzed. The paper focuses on the following chain of events. Asymmetrical irradiation of the crater sidewalls causes differential heating of the air over the slopes and therewith a horizontal temperature gradient. This produces a horizontal pressure gradient, which then forces a cross-basin wind toward the sunlit side. Box-and-whiskers plots are shown to evaluate the relationships among the individual links of the above chain. We then investigate the diurnal evolution for 12 October 2006. In addition to the cross-basin flows at the crater floor that are driven by horizontal temperature gradients, we present a case of elevated cross-basin flows caused by the presence of an elevated inversion layer. The occurrence of a cross-valley flow at the bottom boundary of an elevated inversion layer was previously hypothesized in a conceptual model (Vergeiner and Dreiseitl 1987) and was further confirmed in a modeling study (Lehner and Gohm 2010).

2. Measurements and data analysis

Arizona's Meteor Crater is located 40 km east of Flagstaff, Arizona. The nearly circular basin of the crater, which was produced about 50 000 yr ago by the impact of a meteorite (Kring 2007), is 1.2 km in diameter at rim level and has a depth of 165 m. Its rim rises 30–50 m above the surrounding plain.

In October 2006 the Meteor Crater Experiment (METCRAX) took place inside and in the immediate vicinity of the crater basin. A thorough description of the instrumentation, the measurement sites, and the data has already been published (Whiteman et al. 2008), so that a detailed description of the data used in this study can be omitted here. Table 1 gives a short summary on the instruments relevant for the present paper. For our analysis we use slope-parallel global radiation, temperature, pressure, and wind data from six Integrated Surface Flux Facility (ISFF) towers, one on the west crater rim, one in the center of the crater floor, and two on the east and west sidewalls, respectively; data from temperature dataloggers that were installed at a height of 1.2 m AGL on east–west and north–south lines through the crater; and temperature and wind data from three tethered balloons flown along an east–west line during an intensive observing period (IOP) on the morning of 23 October. Instrument locations are shown in Fig. 2. At the ISFF towers, temperature and wind measurements were taken at several vertical levels

TABLE 1. Instrumentation characteristics (additional information online at http://www.eol.ucar.edu/isf/projects/METCRAX/isff/).

	Instrument	Accuracy	Sampling rate	Averaging period (min)
Global radiation	Eppley pyranometer	± 5 W m^{-2} or 5%	0.2 s^{-1}	5
Temperature	Vaisala 50Y hygrothermometer (EL, EU)	NCAR calibration: ± 0.2°C	1 s^{-1}	5
	NCAR hygrothermometer (WL, WU)	NCAR calibration: ± 0.1°C	1 s^{-1}	5
	HOBO Pro Temp/Ext Temp temperature dataloggers	Appendix: ± 0.71°C	5 min	—
Pressure	Vaisala PTB barometer	Manufacturer: ± 0.25 hPa	1 s^{-1}	5
Wind	CSAT3 sonic anemometer	Manufacturer: ± 0.04 m s^{-1}	60 s^{-1}	5

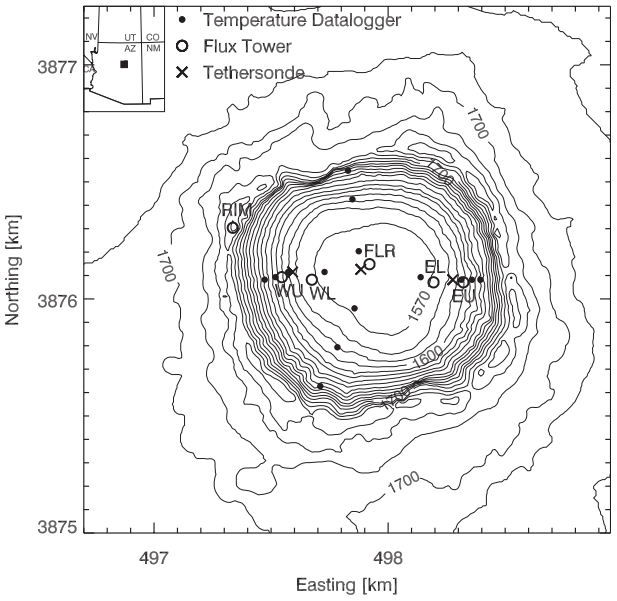

FIG. 2. Location of instrumentation in Arizona's Meteor Crater used in the analyses. Universal transverse Mercator grid 12S with 10-m contour interval. The black square in the small upper-left figure shows the location of the Meteor Crater.

between 0.5 and 10 m; pressure was measured at 2 m. Most of the temperature measurements from the towers used in this study were made with aspirated temperature sensors. Sensors in the temperature dataloggers and the temperature sensor at the east upper tower, however, were exposed in unaspirated radiation shields. The appendix describes the method used to correct these measurements for the amount of overheating that occurred during daytime, predominantly during periods with low wind speeds. The overall uncertainty of the corrected temperature data is about ±1°C.

This paper focuses on the thermally driven wind circulations between 0600 and 2000 mountain standard time (MST) during periods of calm background winds within the 30-day experimental period, when asymmetric insolation was expected to have the greatest impact on the evolution of the wind field. In contrast, days with strong background winds were characterized by easterly winds within the crater basin during the entire day. These periods of prevailing easterly winds coincided with mostly westerly winds at the crater rim, suggesting the formation of an eddy the size of the crater basin. The strong background winds influenced the entire crater atmosphere, disturbing the evolution of the thermally driven flows. In these events temperature differences between the opposing sidewalls were reduced due to strong mixing. Pressure measurements on the east and west sidewalls corresponded to the wind field, with higher pressure on the east sidewall corresponding to a downward-directed (downslope) airflow, and lower pressure on the west sidewall corresponding to an upward-directed (upslope) airflow. East–west pressure differences were generally higher during strong wind periods than during calm wind periods. To exclude these events of strong background winds from the analysis of the 30 days of data, we applied a simple filter to the data. An upper threshold of 4 m s^{-1} was introduced for the wind speeds at the western crater rim. Data collected at times when the threshold was exceeded or within ±15 min of a data point exceeding the threshold were not included in the analyses. The 4 m s^{-1} threshold is chosen somewhat arbitrarily. Different thresholds (3 and 5 m s^{-1}) were also considered, but rejected for different reasons. Six days (11, 12, 19, 22, 23, and 28 October) that exhibited a near-ideal evolution of temperature asymmetries and wind direction were selected by eye from the 30-day dataset. Parts of the analysis were redone for this data subset. The agreement between the results for the 6-day selection and all three thresholds was qualitatively good, suggesting that the use of a fixed wind threshold is a valid approach. The 3 m s^{-1} threshold, however, excluded the greater part of the data points, thus significantly reducing the dataset. Even during the six selected days many data points were rejected so that no single day remained with complete data. The 5 m s^{-1} threshold, on the other hand, included several data points in the close vicinity of high wind speed events that were clearly influenced by the background wind. Results using the ±15-min interval were compared to results using a longer time range, where data within 2 h after a data point exceeding the wind threshold were omitted. The use of the longer time interval, however, did not produce any substantial differences in the results. Hereafter, this new data subset (i.e., the entire 30-day dataset with the 4 m s^{-1} threshold), which contains about 30%–40% of the complete dataset, will be referred to as *filtered data*.

3. Mean diurnal evolution

a. Radiation difference

Filtered diurnal cycles of the difference in slope-parallel global radiation between the east and west sidewalls $(\Delta R)_{EW}$ at the lower-altitude tower sites (EL–WL) and the upper-altitude tower sites (EU–WU), averaged over the period from 1 to 30 October, are shown in Fig. 3a. The standard deviation for $(\Delta R)_{EW}$ lies below 200 W m^{-2} except for an approximately 2-h period in the afternoon, when it increases for the upper-altitude sites to 300 W m^{-2} (not shown). The onset of a difference in slope-parallel global radiation occurred along with sunrise at the west sidewall. Approximate times of local sunrise and sunset at the four tower sites are listed in Table 2. The absolute

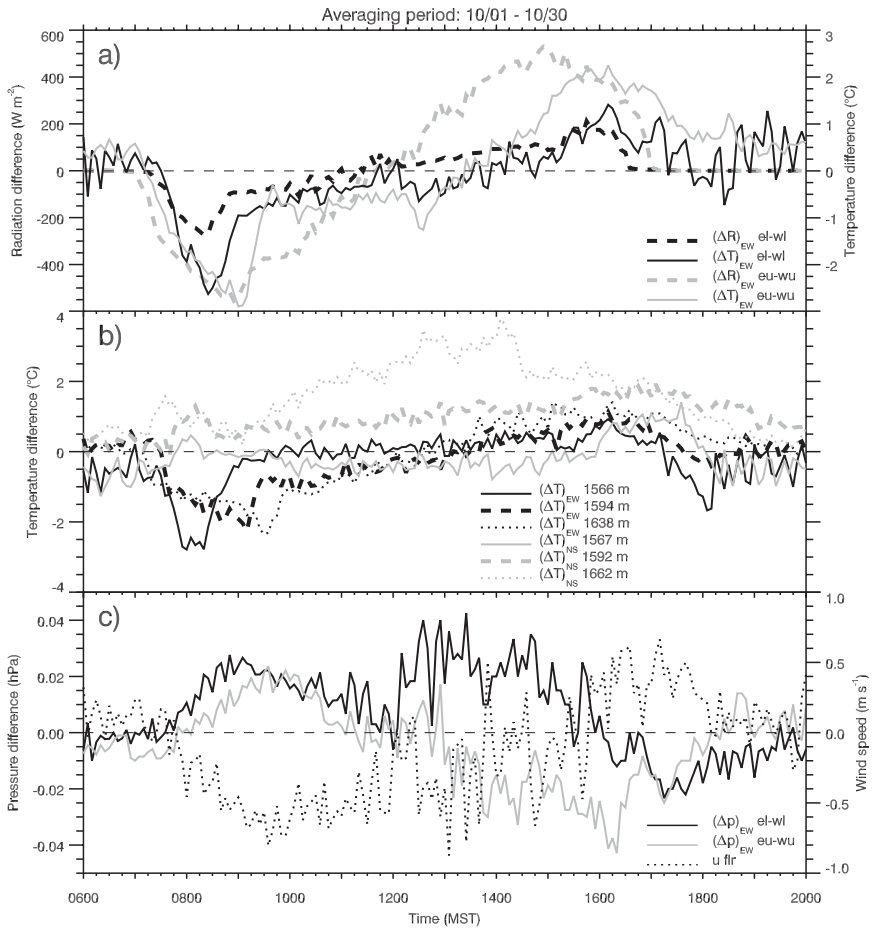

FIG. 3. Diurnal evolution of (a) the differences in slope-parallel global radiation (W m^{-2}) and temperature (°C) between the east and west sidewalls at the lower- and upper-altitude tower sites, (b) the temperature differences between the north and south sidewalls at various altitudes, and (c) the pressure differences (hPa) at 2 m AGL between the east and west sidewalls, and also the east–west wind component (m s^{-1}) at the crater floor center at 2 m AGL. Temperature differences are at 0.5 m AGL in (a) and at 1.2 m AGL in (b). See Table 3 for the exact heights of the measurement sites used to compute the differences. All curves are averaged over the 1–30 Oct period filtered data. For better comparison the computation of averages between EU and WU and between EL and WL, respectively, includes only those data points for which all (i.e., radiation, temperature, and pressure difference) filtered data were available for the respective pair.

difference starts to increase earlier between the upper-altitude sites, consistent with the earlier onset of irradiation at WU relative to WL, exceeding an absolute value of 10 W m^{-2} between EU and WU at 0705 MST and between EL and WL at 0720 MST. At about 1100 (EL–WL) and 1140 MST (EU–WU) the sign changes and the east sidewall becomes more strongly illuminated. The morning period [with the west sidewall more strongly illuminated and negative values of $(\Delta R)_{EW}$] is shorter than the evening period [with the east sidewall being more strongly illuminated and positive values of $(\Delta R)_{EW}$]. The maximum magnitude of $(\Delta R)_{EW}$, however, is very similar in the morning and afternoon at both altitudes. Between the low-altitude sites the morning minimum amounts to −274 W m^{-2} and the evening maximum to 212 W m^{-2}. At the more steeply inclined upper-altitude sites, the maximum values of the absolute difference are about 2 times as high, with 555 and 530 W m^{-2},

TABLE 2. Approximate times of local sunrise and sunset at sites WU, WL, EL, and EU. The first number gives the time for 1 Oct and the second time is for 30 Oct. Sunrise and sunset were determined from observations of global radiation at the respective sites.

Site	Sunrise (MST)	Sunset (MST)
WU	0655/0720	1520/1445
WL	0715/0745	1555/1515
EL	0815/0850	1710/1630
EU	0850/0910	1725/1645

respectively. These morning and evening differences are remarkably similar, even though the instrument planes of the pyranometers deviated from pure westerly and easterly exposures (Hoch and Whiteman 2010).

b. Temperature difference

Temperature differences $(\Delta T)_{EW}$ between EL and WL and between EU and WU show a diurnal cycle that is similar to the difference in slope-parallel global radiation (Fig. 3a). The pronounced diurnal evolution observed during clear-sky days is seen in these monthly means. Although the times of sunrise and sunset, and therefore the times of maximum heating of the respective sidewalls, change slightly with time of the year (Table 2), the 1-month period is short enough that the time shift has little broadening effect on the maxima in the averaged curves. The onset of the radiation and temperature differences in the morning varies by about 30 min and equally for the end of the radiation difference in the evening. The end of the temperature difference in the evening is generally less abrupt making it difficult to state the variation with time. A pronounced east–west temperature gradient develops shortly after the onset of a radiation contrast, particularly in the morning. In the evening, however, temperature differences persist for a longer time, continuing even after sunset at the east sidewall. Also, the decrease is smoother than the decrease in $(\Delta R)_{EW}$. The magnitude of $(\Delta T)_{EW}$ seems to be strongly linked to the magnitude of $(\Delta R)_{EW}$. Highest differences in slope-parallel global radiation and temperature occur between the two upper-altitude tower sites. Standard deviations stay mostly below or around 1°C. Only in the morning before 0800 MST and in the evening after 1800 MST do several peaks occur in the standard deviation for EL-WL reaching up to 2°C (not shown). It should also be mentioned that $(\Delta T)_{EW}$ decreases with height above the surface at most levels and loses its pronounced diurnal cycle. The morning minimum at 5 m AGL is weaker by a factor of about 3.5–4 than at 0.5 m AGL and temperatures at the east side are warmer than on the west side during most of the remaining day. The two curves thus show the strongest relation using temperature measurements at 0.5 m AGL (Fig. 3a).

Figure 3b shows the filtered monthly mean diurnal cycle of the temperature difference between temperature sensors at the east and west sidewalls $(\Delta T)_{EW}$ and at the north and south sidewalls $(\Delta T)_{NS}$, respectively, at various altitudes. Temperature differences are calculated between pairs of temperature sensors located at similar altitudes on opposing sidewalls (Table 3). The biggest height deviation between pairs of sensors is 9.5 m (EW 1638 m). We found that $(\Delta T)_{EW}$ at 1566 m MSL and $(\Delta T)_{NS}$ at 1567 m MSL are more representative of temperature differences across the crater floor than between crater sidewalls. Standard deviations are again mostly below 1°C (not shown), except for the morning and evening, when individual peaks reach up to 2°C for the temperature differences near the crater floor [$(\Delta T)_{EW}$ at 1566 m MSL and $(\Delta T)_{NS}$ at 1567 m MSL]. Averaged $(\Delta T)_{EW}$ reaches a first maximum (absolute values) in the morning between about 0800 and 0930 MST, with the east-facing (west) slope being warmer than the west-facing (east) slope. Morning temperature differences exceed 4°C at the lowest elevation (1566 m MSL) on several days (not shown). In the early afternoon the west-facing sidewall becomes warmer than the east-facing sidewall, reaching its maximum around 1600 MST. Interestingly, the maximum in the late afternoon is weaker than the maximum in the morning at all temperature datalogger and tower sites. While $(\Delta T)_{EW}$ at 1566 m MSL reaches 0°C by about 0900 MST and remains at that level for the next 5 h, the east-facing sidewall continues to be warmer than the west-facing sidewall at 1594 and 1638 m MSL until about 1300 MST, with $(\Delta T)_{EW}$ increasing linearly during this time. This slow linear increase is also observed in $(\Delta R)_{EW}$ between EL and WL (Fig. 3a). Between EU and WU, however, the increase of $(\Delta R)_{EW}$ is far steeper than in any of the temperature differences, which probably relates to vertical mixing of the crater atmosphere during daytime so that local temperatures at the sidewalls, and therewith $(\Delta T)_{EW}$, are not completely independent from the rest of the crater atmosphere.

In the north–south direction, the south-facing sidewall is generally warmer than the north-facing sidewall during the entire day except for the lowest analyzed altitude of 1567 m MSL, where $(\Delta T)_{NS}$, although weak, is reversed between 0830 and 1600 MST (Fig. 3b).

TABLE 3. Altitudes of sites on the opposing crater sidewalls used for the calculation of east–west and north–south differences. The heights were determined from a digital elevation model (DEM) using GPS latitude and longitude measurements. Numbers in parentheses give a range of altitudes for different height measurement methods (GPS, DEM, and barometric altitude measurements above the crater floor; information online at http://www.eol.ucar.edu/isf/projects/METCRAX/isff/).

Terminology for the differences	Site and height (m MSL)	Site and height (m MSL)
East–West		
EW 1566 m	E03, 1566	W02, 1567
EW 1594 m	E05, 1597	W04, 1591
EW 1613 m	E06, 1614	W05, 1613
EW 1638 m	E07, 1633	W07, 1643
EL–WL	EL, 1572 (1572–1575)	WL, 1572 (1572–1575)
EU–WU	EU, 1600 (1600–1602)	WU, 1602 (1602–1609)
North–South		
NS 1567 m	N01, 1567	S02, 1567
NS 1592 m	N04, 1595	S04, 1590
NS 1662 m	N07, 1662	S07, 1662

c. Pressure difference

An asymmetry in the pressure field is expected to develop in accordance with the asymmetry in the temperature distribution. Figure 3c shows the filtered averaged east–west pressure difference $(\Delta p)_{\mathrm{EW}}$ between the two lower-altitude and the two upper-altitude tower sites, respectively. In addition to the pressure difference induced by asymmetric heating of the east and west slopes, the vertical pressure gradient contributes to the observed east–west pressure differences because the towers on the east and west sidewalls were not installed at exactly the same height (Table 3). The height deviation amounts to approximately 2 m between the two upper-altitude sites and 0.5 m between the two lower-altitude sites. A simple correction was applied to remove the vertical differences, which are about one order of magnitude higher than the thermally induced horizontal differences. A constant correction value was defined as the mean pressure difference of all data points used for the analysis and subtracted from the total difference. The corrected mean east–west pressure difference exhibits a pronounced diurnal evolution in accordance with the temperature gradient. At the upper altitude the sign of $(\Delta p)_{\mathrm{EW}}$ points in the opposite direction of $(\Delta T)_{\mathrm{EW}}$ during most of the day. At the lower altitude, however, the change of sign occurs somewhat later in the afternoon compared to $(\Delta T)_{\mathrm{EW}}$. But considering the very simple correction of the height differences between the measurement sites and the order of magnitude of the vertical pressure gradient compared to the horizontal gradient as well as the possible impacts of nonthermal effects, this deviation may lie within the range of uncertainty. During the morning and evening the standard deviations for $(\Delta p)_{\mathrm{EW}}$ are below 0.02 hPa (EL–WL) and 0.03 hPa (EU–WU), respectively. During the daytime (from about 1000 to 1700 MST), values are mostly above or around 0.02 hPa with peak values of up to more than 0.06 hPa (not shown).

d. Cross-basin and slope winds

The filtered mean east–west wind component u, measured at 2 m AGL at the tower on the crater floor, is displayed in Fig. 3c. Other vertical levels on the tower (not shown) up to 8.5 m AGL varied little from the 2-m level in wind direction and speed. The diurnal evolution of u is qualitatively in accordance with the east–west radiation, temperature, and pressure differences, with u pointing from the side with lower radiation, lower temperature, and higher pressure to the side with higher radiation, higher temperature, and lower pressure. The change from an easterly to a westerly component takes place between 1400 and 1600 MST. This time of wind shift corresponds more strongly with the diurnal evolution of $(\Delta p)_{\mathrm{EW}}$ between the lower-altitude sites than between the upper-altitude sites. Generally, the east–west wind component seems to be strongly determined by $(\Delta p)_{\mathrm{EW}}$. During several days it responds immediately to changes in the pressure gradient, changing its direction synchronously with the pressure gradient direction (section 5). The diurnal cycle of the standard deviation is very similar to the standard deviation for the pressure difference with values below or around 0.5 m s^{-1} in the morning and evening and values of up to more than 1 m s^{-1} during the day (not shown).

Figure 4 gives an overview of the overall daily wind field inside the crater. Relative frequencies of observed wind directions are plotted for the west slope (WL), the crater center (FLR), and the east slope (EL) for 1-h time periods in the morning (0900–1000 MST), in the afternoon (1400–1500 MST), and in the evening (1700–1800 MST). In the morning, when the west slope is illuminated more strongly by the sun, the predominant wind direction at WL is from the east, indicating upslope winds. A 1-month average of the wind direction at the west slope shows the onset of upslope winds at about 0700 MST together with a sharp increase in near-surface temperature (not shown), coinciding with the time of local sunrise (Fig. 3a). At the same time, southeasterly katabatic winds continue to prevail on the east sidewall. Although the temperature on the east sidewall starts to rise shortly after the temperature on the west sidewall, the average wind direction does not change to upslope until about 0930 MST (not shown). At the crater floor the predominant wind direction is from east or southeast, while the temperature on the west sidewall is still warmer than on the east sidewall and the pressure is therefore higher at the east sidewall (Fig. 3). In midafternoon the east–west temperature and pressure gradients are close to zero, while the south-facing slope is still warmer than the north-facing slope, suggesting higher pressure on the southern side. The wind direction at the crater floor is predominantly from the south during this time. On the west sidewall, upslope winds are still prevailing. On the east sidewall, upslope winds have also developed, indicated by westerly or southwesterly winds. In the early evening, winds on the east-facing sidewall have turned from upslope to westerly or southwesterly katabatic winds. On the west-facing sidewall, however, upslope winds are maintained. With the west-facing side being warmer than the east-facing side and the corresponding east–west pressure gradient pointing to the west, the wind direction at the crater floor shifts to west or southwest.

4. Relation between individual parameters

Box-and-whiskers plots are used to show the relation between pairs of variables. For these plots only daytime

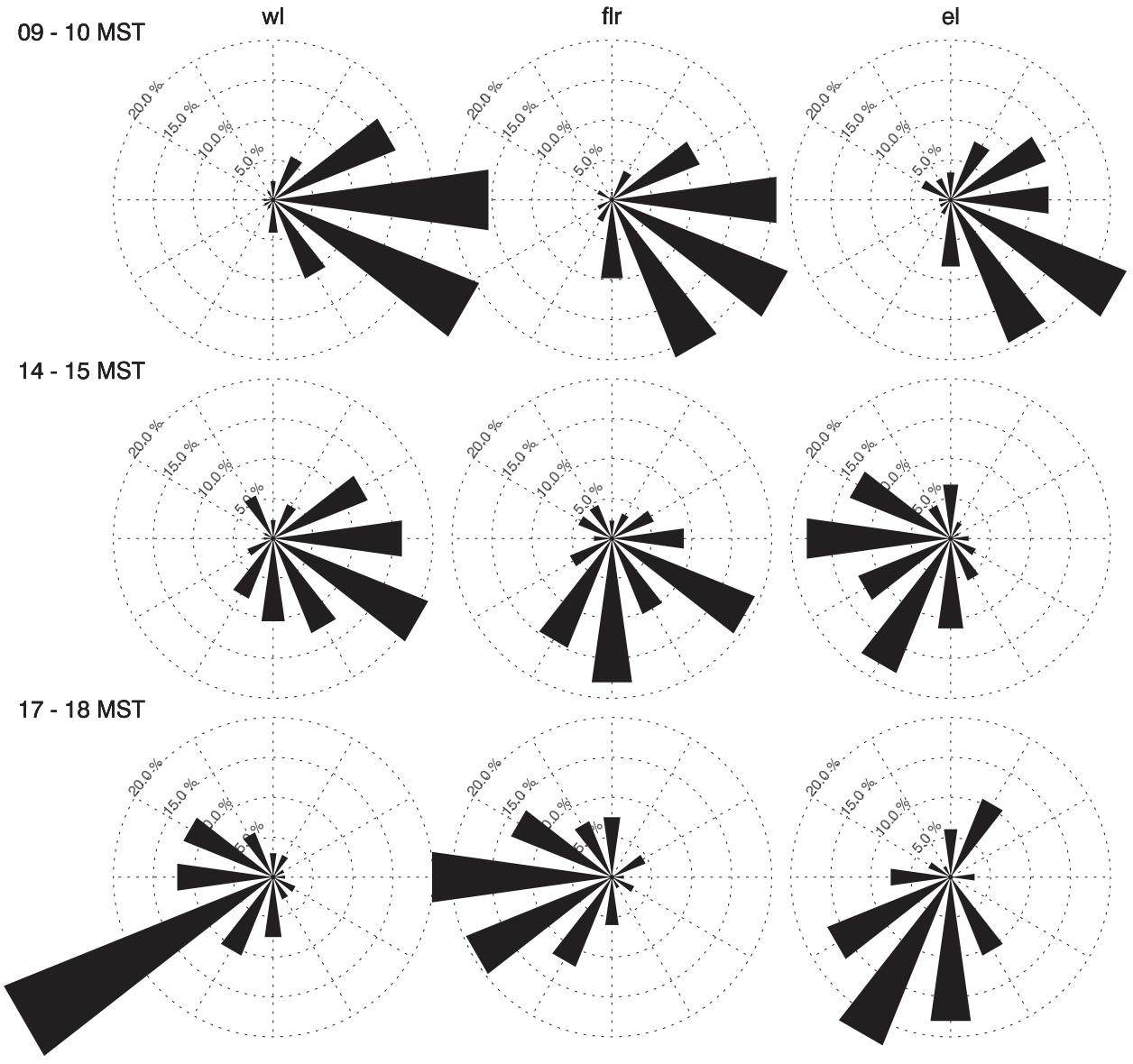

FIG. 4. Relative frequencies of wind directions at 2 m AGL (FLR) and 1.5 m AGL (WL, EL) observed during the 1–30 Oct 2006 period for (top) 0900–1000, (middle) 1400–1500, and (bottom) 1700–1800 MST for (left) WL, (center), FLR, and (right) EL.

filtered data between 0600 and 2000 MST are used (i.e., the same range as for the time series plots). This period includes the entire time between sunrise (around 0700 MST) and sunset (around 1700 MST), but also the time after sunset when there is still a pronounced east–west temperature difference and therefore a forcing for cross-basin winds. For the plot showing the relation between radiation and temperature difference, however, filtered data are limited to the time between 0715 (i.e., approximate sunrise at WL on 1 October) and 1710 MST (i.e., approximate sunset at EL on 30 October; see Table 2).

a. Radiation difference–temperature difference relationship

Temperature differences between EL and WL show a nearly linear relationship to east–west differences in slope-parallel global radiation (Fig. 5). Strongest asymmetries in both irradiation and temperature occur in the morning from 0700 to 0900 MST and in the evening from 1500 to 1700 MST. Data points between 0900 and 1500 MST occur close to $(\Delta R)_{\mathrm{EW}} = 0$ W m^{-2}, centered around 1200 MST. The $(\Delta R)_{\mathrm{EW}} = -150$ W m^{-2} bin is clearly an outlier from

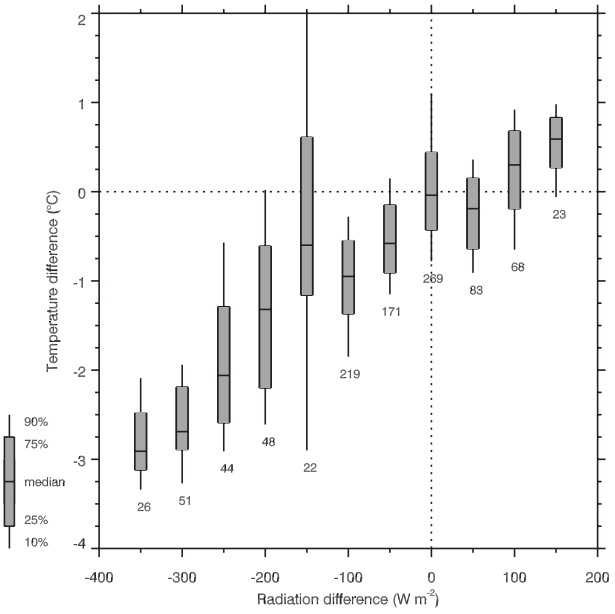

FIG. 5. Relation between the east–west slope-parallel global radiation differences (W m^{-2}) and the east–west temperature difference (°C) measured between sites EL and WL. Boxes are plotted in the center of each 50 W m^{-2} radiation category. Horizontal black lines in the middle of the boxes indicate the median of the temperature difference for the respective radiation difference category. Gray-shaded boxes and whiskers show the lower and upper quartiles and 10th and 90th percentiles, respectively. The number below each box gives the number of data points per bin. Temperature data are at 0.5 m AGL. Only filtered data between 0715 (i.e., approximate sunrise at site WL on 1 Oct) and 1710 MST (i.e., approximate sunset at site EL on 30 Oct) are used.

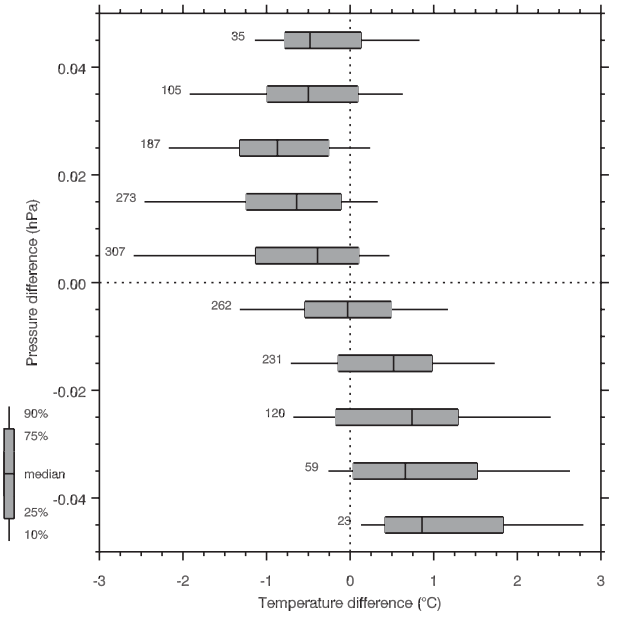

FIG. 6. Relation between the east–west temperature (°C) and pressure (hPa) differences measured between sites EL and WL. Temperature data are at 0.5 m AGL and pressure data are at 2 m AGL. Filtered data from 0600 to 2000 MST are used.

the rest of the data. This strong deviation to high temperature differences is caused by a few strong $(\Delta T)_{EW}$ values and the fact that the respective $(\Delta R)_{EW}$ range contains fewer data points than other ranges. The $(\Delta R)_{EW}$ range seems to correspond to a short transition between strong radiation differences in the morning and smaller differences during the day. Similarly, the area close to $(\Delta R)_{EW} = 150$ W m^{-2} contains comparatively few values.

An additional means of characterizing the relationship between $(\Delta T)_{EW}$ and $(\Delta R)_{EW}$ is to determine the number of data points having the same sign for both $(\Delta R)_{EW}$ and $(\Delta T)_{EW}$, corresponding to the lower-left and upper-right quadrants in Fig. 5. At the lower-altitude sites, 78% of the data points have the same sign, and at the upper-altitude sites, 73% have the same sign (not shown).

b. *Temperature difference–pressure difference relationship*

The east–west pressure gradient tends to oppose the east–west temperature gradient (Fig. 6). The signs of $(\Delta T)_{EW}$ and $(\Delta p)_{EW}$ between EL and WL differ in 71% of the data points, and between EU and WU (not shown) in 58% of the data points. A few outliers of $|(\Delta p)_{EW}| \geq 0.1$ hPa occur with low absolute temperature differences. These outliers, which are not shown in Fig. 6, were mostly caused by short calm events between periods of wind speeds outside the crater that exceeded the 4 m s^{-1} threshold and are, thus, not entirely representative for the nondisturbed, thermally driven crater atmosphere. In contrast to the relations between $(\Delta R)_{EW}$ and $(\Delta T)_{EW}$ and between $(\Delta p)_{EW}$ and u (sections 4a and 4c), the relation between $(\Delta T)_{EW}$ and $(\Delta p)_{EW}$ is nonlinear. The relation between local temperature and pressure differences between individual measurement sites on the opposing east and west sidewalls was compared to the relation between local pressure differences and vertically averaged east–west temperature gradients. The use of vertically averaged temperature gradients instead of absolute point differences was an attempt to take into account that the pressure difference at a certain height is caused by temperature differences in the vertical column above this level. But the averaging led only to an improvement of the relation at small, negative pressure differences (not shown) and the number of data points with opposing signs changed by only a few percent.

c. *Relationship between pressure difference and east–west wind component*

The final link in the relationship between asymmetric insolation and cross-basin winds is the relation between

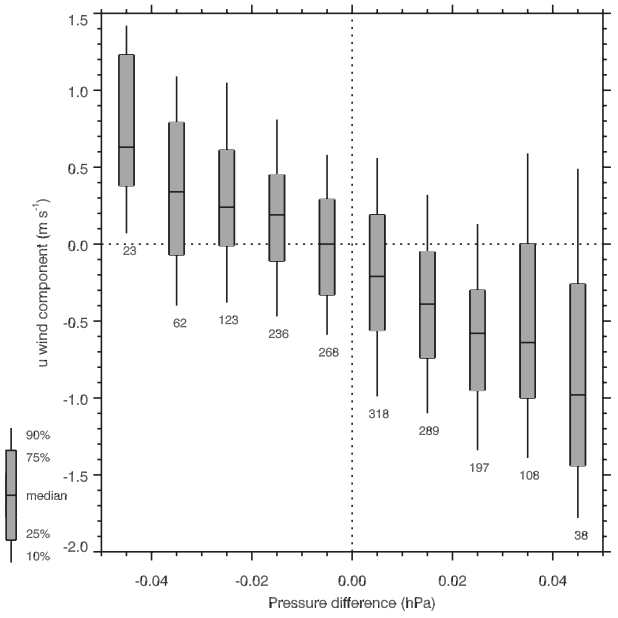

FIG. 7. Relation between the east–west pressure difference (hPa) and the east–west wind component (m s^{-1}) at 2 m AGL in the center of the crater floor. Here, $(\Delta p)_{EW}$ is calculated between sites EL and WL for the filtered data from 0600 to 2000 MST.

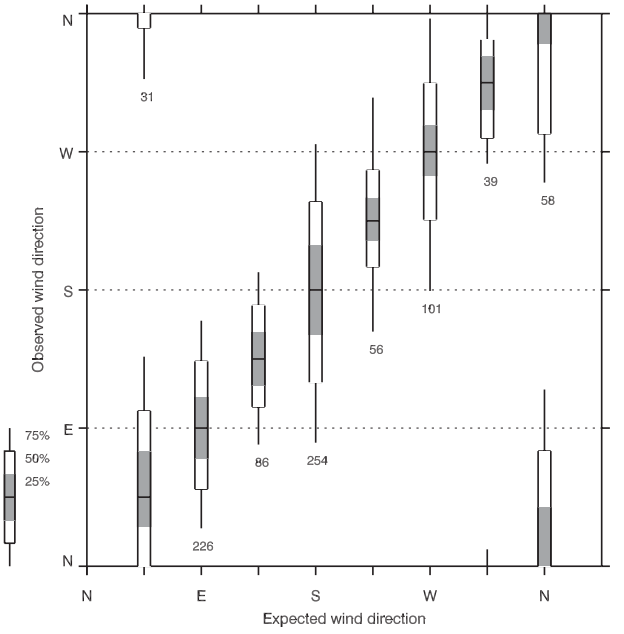

FIG. 8. Relation between the observed wind direction at the 2 m AGL level of the central tower and the expected wind direction derived from the north–south and east–west temperature differences. See text for details on the determination of the expected wind direction. Horizontal black lines in the middle of the boxes give the expected wind direction for the respective category. Gray-shaded boxes, white boxes, and whiskers show the ranges of observed wind direction within which 25%, 50%, and 75% of all the data in this category lie.

the pressure gradient and the cross-basin wind. The 2-m east–west wind component u at the basin floor and $(\Delta p)_{EW}$ (Fig. 7) show a better relation than $(\Delta T)_{EW}$ and $(\Delta p)_{EW}$ (Fig. 6). The highest wind speeds are observed when $(\Delta p)_{EW}$ is strongest, and the winds blow mainly from the high pressure side toward the low pressure side of the crater, as expected. In 68% of all the data points, $(\Delta p)_{EW}$ and u have an opposing sign, corresponding to the upper-left and lower-right quadrants in Fig. 7. The medians of the respective pressure difference categories indicate a linear relation between u and $(\Delta p)_{EW}$. The slope of the line, however, is smaller at $(\Delta p)_{EW} < -0.02$ hPa than at $(\Delta p)_{EW} > -0.02$ hPa. Some outliers (not shown in Fig. 7), which were also seen in the relation of temperature and pressure differences and are caused by the short break-ins of strong winds from outside the crater, occur mainly with high positive pressure differences and negative (i.e., easterly) wind components.

d. Temperature difference–wind direction relationship

To further test the relationship between the cross-basin wind and the temperature gradient, the observed wind direction at the crater floor is compared with the expected wind direction derived from the observed temperature differences in the east–west and north–south directions (Fig. 8). Since no pressure measurements are available for the north and south sidewalls, the wind direction can only be compared to the temperature differences. The expected wind direction indicates the wind that blows from the colder toward the warmer sidewall along the horizontal temperature gradient. For its determination eight classes of wind direction were defined and the following simple criterion was used. If, for example, $(\Delta T)_{EW}$ exceeds 1°C but $(\Delta T)_{NS}$ is below this threshold, the expected wind direction is either E or W according to the sign of $(\Delta T)_{EW}$. If both $(\Delta T)_{EW}$ and $(\Delta T)_{NS}$ exceed 1°C, the expected wind is either from the northeast (NE), southeast (SE), southwest (SW), or northwest (NW), according to the signs of $(\Delta T)_{EW}$ and $(\Delta T)_{NS}$. Thus, for example, if the north slope is warmer than the south slope by at least 1°C and the west slope is warmer than the east slope by at least 1°C, then the expected wind is from the SE. Filtered temperature data from dataloggers at 1578 (south slope) and 1576 m MSL (north slope) were used to determine $(\Delta T)_{NS}$, as these heights agreed best with the flux tower heights at WL and EL (1572 m MSL).

Figure 8 shows that in most categories the observed wind directions agree fairly well with the wind direction expected from the horizontal temperature gradient. The largest scatter occurs for northerly and southerly expected

winds, in which the 75% whiskers span a range of more than 180°. Except for these two categories and the NE class, the 50% boxes lie within a range of less than 90°. The most data (254 points) are contained in class S with the data distributed comparatively homogeneously over all wind directions.

5. Case study: 12 October

On 12 October, winds above the crater are predominantly from the east. They shift from a southwesterly direction to east at approximately 0800 MST and back again to southwest at about 2000 MST. The nocturnal southwesterly wind direction is the result of a drainage flow that forms on the slightly sloping plain surrounding the crater during synoptically undisturbed nights (Whiteman et al. 2008). At the crater rim, wind speeds drop to zero as the wind shifts to an easterly direction, but shortly afterward they increase again (Fig. 9a). Wind speeds range from about 3 to 5 m s^{-1} during most of the day, although they drop frequently below this level during an approximately 3-h period in the afternoon. The morning surface inversion in the crater basin is comparatively weak with a temperature increase of roughly 2°–4°C over a vertical distance of about 30 m (not shown).

The east–west temperature difference between the two lower-altitude tower sites follows the evolution of $(\Delta R)_{EW}$ closely in the morning and also during the day (Fig. 9b). Unfortunately, no radiation data are available during the evening temperature difference maximum. Between the two upper-altitude sites the timing of the maximum and minimum of $(\Delta T)_{EW}$ match the respective timing of the maximum and minimum of $(\Delta R)_{EW}$, but in contrast to slope-parallel global radiation, the temperature difference quickly returns to above −2°C. Only in the afternoon does it show an increase similar to that of $(\Delta R)_{EW}$.

The east–west temperature differences at 1566 and 1613 m MSL, respectively, and the north–south temperature differences at 1567 and 1592 m MSL are shown in Fig. 9c. The minimum value for $(\Delta T)_{EW}$ at 1566 m MSL is reached at 0820 MST with −3.8°C and then $(\Delta T)_{EW}$ increases rapidly to 0°C. At 1613 m MSL, $(\Delta T)_{EW}$ also reaches a first minimum shortly after 0800 MST, but then has a second and third, stronger minimum (−2.5° and −2.4°C) a half hour to an hour later. Additional temperature difference curves from various altitude levels (not shown) indicate a continuous broadening of the minimum with height. This is apparently caused by the continuous retreat of the shadow from the crater floor toward the east rim, leading to later temperature rises at the higher elevations. Afterward, $(\Delta T)_{EW}$ increases nearly linearly toward 0°C at 1613 m MSL. In the evening, $(\Delta T)_{EW}$ reaches its maximum at about 1615 MST at both heights, with 1.5° and 2.5°C at 1566 and 1613 m MSL, respectively. After the evening maximum, the temperature difference at 1566 m MSL changes sign again and becomes negative, reaching −3.5°C. Strong temperature differences, both positive and negative, occur during many nights, often changing very rapidly between positive and negative. We believe that these nocturnal temperature differences result from a movement of the surface inversion that is pushed down on one side. But this phenomenon including the mechanism that pushes down the inversion still needs further analysis. Intrusions of cold air coming over the crater rim are known disturbances of the nocturnal crater atmosphere (Whiteman et al. 2010).

The east–west pressure difference between the lower-altitude and the upper-altitude tower pairs remains near zero during the morning (Fig. 9d), although $(\Delta T)_{EW}$ has minima at the respective sites (Fig. 9b). Shortly after the temperature difference has returned to about 0°C (EL–WL) or to above −2°C (EU–WU), respectively, $(\Delta p)_{EW}$ increases slightly and reaches positive values of approximately 0.03 hPa. The pressure on the west sidewall becomes higher than on the east sidewall at the upper-altitude sites shortly before 1000 MST, which then continues until approximately 2000 MST, with $(\Delta p)_{EW}$ of up to −0.15 hPa. At the lower-altitude sites, however, $(\Delta p)_{EW}$ alternates between positive and negative values until the late afternoon, when $(\Delta T)_{EW}$ between EL and WL increases sharply. After about 1730 MST, $(\Delta T)_{EW}$ and $(\Delta p)_{EW}$ return again to values close to 0°C and 0 hPa at both levels.

The diurnal evolution of the east–west wind component at the crater floor (Fig. 9e) is strongly determined by $(\Delta p)_{EW}$ between EL and WL. This becomes particularly obvious in the early afternoon, when the various peaks in u can be easily matched with the respective peaks in $(\Delta p)_{EW}$. The absolute u minimum value (i.e., an easterly wind component) shortly after 1400 MST, for instance, corresponds to the absolute maximum in $(\Delta p)_{EW}$ (i.e., higher pressure on the east side) occurring at the same time. Likewise, the positive peak in u preceding the minimum corresponds to a relative minimum in $(\Delta p)_{EW}$, which, however, is near zero and does not indicate higher pressure on the west sidewall. But it should be remembered that the dominating vertical pressure gradient has been removed via a constant value, so that absolute pressure differences do not necessarily reflect absolutely correct conditions, but that it is rather the relative tendencies that contain the most valuable information. Also, in the morning u develops a clear easterly direction, although $(\Delta p)_{EW} \approx 0$ hPa. In the evening, however, a constantly westerly component predominates along with the negative $(\Delta p)_{EW}$ that then drops to about 0 m s^{-1}. The north–south wind component v shows mostly a southerly

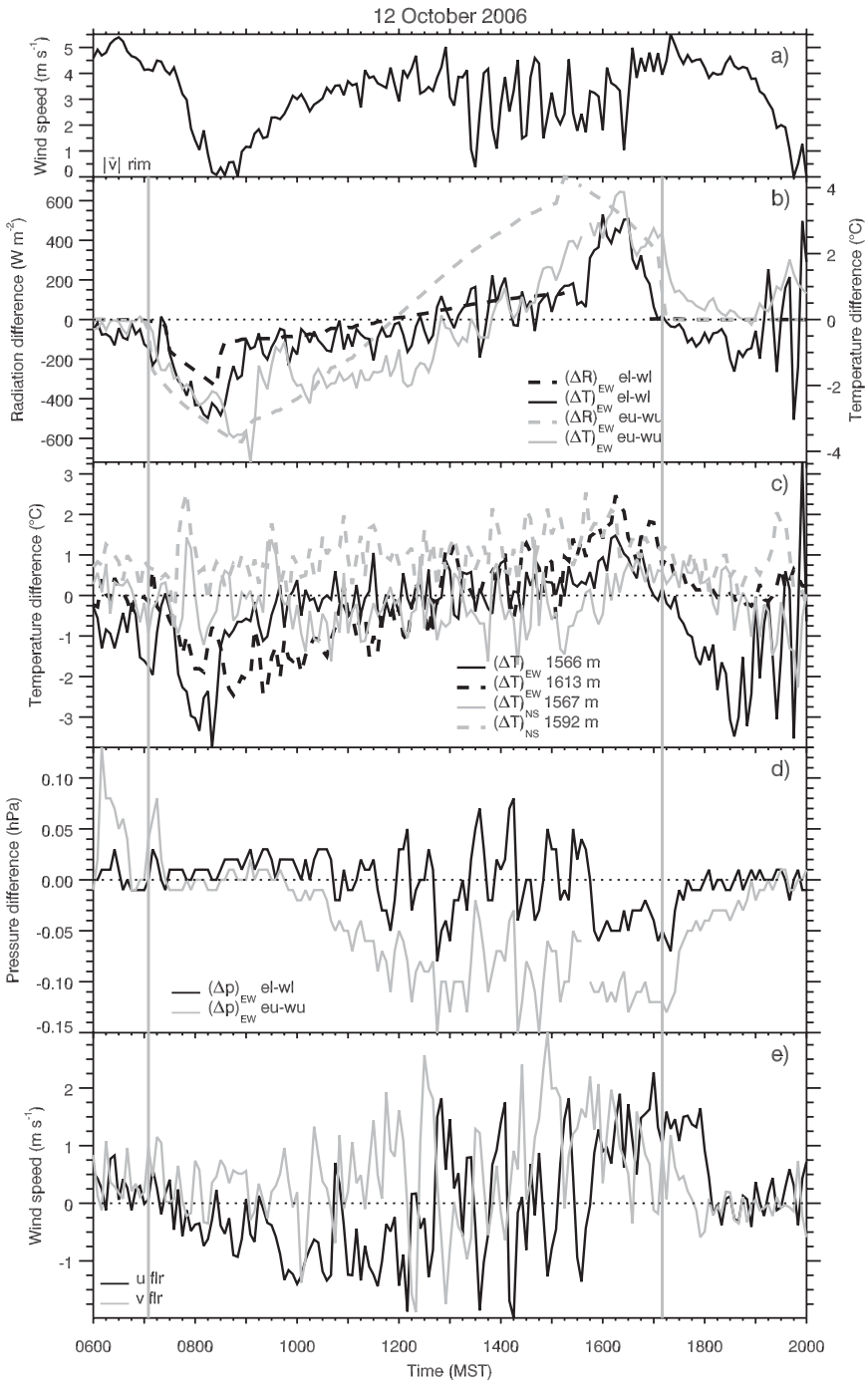

FIG. 9. Time series for 12 Oct: (a) wind speeds (m s^{-1}) at 10 m AGL at the west rim tower, (b) slope-parallel radiation (W m^{-2}) and 0.5 m AGL temperature (°C) differences between the east and west towers at the upper and lower altitudes, (c) east–west and north–south temperature differences (°C) between temperature sensors at two different heights, (d) pressure (hPa) differences between the east and west towers at the upper and lower altitudes, and (e) east–west and north–south wind components (m s^{-1}) at the 2 m AGL level of the central tower. Vertical lines indicate the beginning and end of slope-parallel global radiation contrasts between EU and WU for which $|\Delta R| > 5$ W m^{-2}.

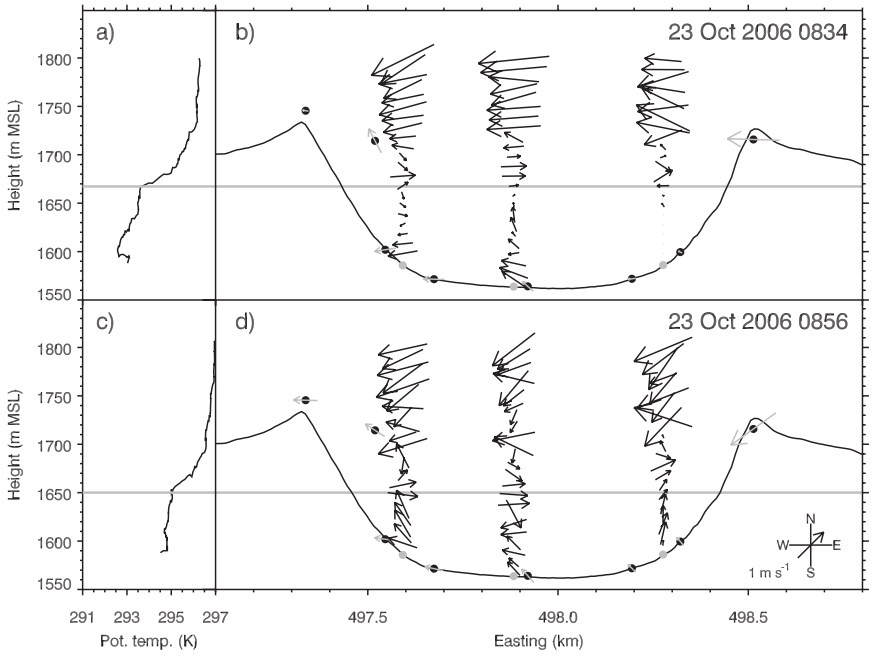

FIG. 10. (a),(c) Potential temperature profiles from the west tethersonde and (b),(d) the horizontal wind field in an east–west cross section through the crater basin at (top) 0834 and (bottom) 0856 MST 23 Oct. Gray arrows show wind measurements from tower sites indicated by black dots. Black arrows show wind measurements from the tethersondes launched from the three sites indicated by the gray dots. Wind arrows from the flux towers are 15-min averages. The locations of the various measurements sites are projected to the east–west cross section.

component during the whole day with occasional shifts to a northerly direction.

6. Elevated cross-basin flow

During several IOPs, tethersondes were flown concurrently from the center of the crater floor and from the west and east sidewalls (Fig. 2). The tethersonde ascents, conducted at sites on an east–west cross section through the crater basin, yield a two-dimensional view of the wind field across the crater during the morning transition period. Figure 10 shows the potential temperature profile (west tethersonde) and the wind field from two soundings on the morning of 23 October. The 0834 MST sounding (Figs. 10a and 10b) shows a westerly cross-basin flow in the elevated inversion above a shallow neutral layer between 1670 and 1700 m MSL. At the top of this layer the wind direction changed again to an easterly flow. Twenty-two minutes later, the bottom of the inversion layer had descended to 1650 m MSL (Figs. 10c and 10d). Accordingly, the layer of westerly winds descended to about the same height. The depth of this layer coincides approximately with the depth of the elevated inversion layer. By the next ascent at 0913 MST (not shown) the inversion depth decreased to about 10 m and the westerly cross-basin flow layer disappeared.

Vergeiner and Dreiseitl (1987) presented a conceptual model that shows that the mass flux in an upslope-wind layer is proportional to the vertical potential temperature gradient in the valley atmosphere. In the presence of an elevated inversion layer the upslope mass flux decreases and a cross-valley flow occurs at the lower boundary of the inversion (see Fig. 1). Vergeiner and Dreiseitl describe the volume flux in the upslope-wind layer by

$$VD = \frac{\dfrac{H}{\tan\alpha}(1 - Q)}{\rho c_p \dfrac{d\theta}{dz}}, \tag{1}$$

where V is the slope-parallel wind component in the slope-wind layer, D is the slope-normal depth of the slope-wind layer, H is the vertical sensible heat flux, α is the slope angle, Q is the fraction of H that goes directly to the valley atmosphere, ρ is the air density, c_p is the heat capacity, and $d\theta/dz$ is the vertical potential temperature gradient of the valley atmosphere. Applying (1) to the elevated inversion layer and the layer below the inversion

allows the calculation of a difference in the mass flux of the slope-wind layer. We can then assume that the residual mass forms the cross-basin flow below the inversion layer and compare the result with the observed strength and depth of this flow. We further assume that $(H/\tan\alpha)(1 - Q)/\rho c_p$ is constant with height so that the difference can be written as

$$\Delta(VD) = \frac{H}{\tan\alpha}(1-Q)\frac{}{\rho c_p}\left[\frac{1}{\left(\frac{d\theta}{dz}\right)_2} - \frac{1}{\left(\frac{d\theta}{dz}\right)_1}\right]$$

$$= \left(VD\frac{d\theta}{dz}\right)_1\left[\frac{1}{\left(\frac{d\theta}{dz}\right)_2} - \frac{1}{\left(\frac{d\theta}{dz}\right)_1}\right], \qquad (2)$$

where the index 1 denotes the lower layer and the index 2 the inversion layer. The tethersounding from the west sidewall and measurements from WU can be used to estimate D and V, respectively. In strict terms, (2) is only applicable to homogenous parts of the sidewall without entrainment or detrainment (Vergeiner and Dreiseitl 1987), which is not true for the Meteor Crater, where the slope angle α changes with height. Since the upper part of the crater sidewalls is steeper than the lower part, our estimate of VD based on observations at the lower sidewall may not be entirely representative for VD at the altitude of the inversion layer either.

The slope-parallel wind component in the upslope wind layer was rather constant at approximately 1 m s^{-1} during the morning of 23 October. At 0834 MST the static stability below the elevated inversion was about 0.016 K m^{-1}, while within the inversion $(d\theta/dz)_2 \approx 0.06$ K m^{-1} (Fig. 10a). The vertical depth of the slope wind layer determined from the west sidewall tethersounding was approximately 40 m. Using a slope angle $\alpha \approx 24°$, which is representative for WU and the launch site of the tethersonde, $(VD)_1 = 36$ m^2 s^{-1}. Inserting these figures into (2), we can derive $\Delta(VD) \approx -26$ m^2 s^{-1}. From Fig. 10b we can also determine a rough estimate of the cross-basin wind speed u and the depth of the cross-basin flow layer, δ. With $u \approx 1$ m s^{-1} and $\delta \approx 20$ m, the cross-basin volume flux amounts to 20 m^2 s^{-1} ($\delta \approx 20$ m is slightly less than the actual cross-basin flow-layer depth, but takes into account that u is not constant over the entire depth but decreases toward the upper and lower boundaries), which is very close to our approximation using (2). At 0800 MST (not shown) the results are equally close with $\Delta(VD) \approx -7$ m^2 s^{-1} and $u\delta \approx 10$ m^2 s^{-1}. At 0856 MST (Figs. 10c and 10d), however, the results differ more strongly with $\Delta(VD) \approx -68$ m^2 s^{-1} and $u\delta \approx 30$ m^2 s^{-1}. Clearly, this is only a very rough estimate of both the change of volume flux in the slope wind layer and the volume flux in the cross-basin flow layer. The generally good agreement suggests that the elevated cross-basin wind layer is a result of the inversion according to Vergeiner and Dreiseitl's (1987) conceptual model. However, the observed cross-basin circulation at the height of the inversion layer may be further enhanced by the presence of an easterly wind above the crater, which produces a second vortex above the inversion layer, counterrotating to the lower, thermally driven vortex.

7. Discussion

a. Response time

The cross-basin winds at the crater floor are enforced by a horizontal pressure gradient that develops due to asymmetric solar heating of the crater sidewalls. We may write the horizontal equation of motion for the u component as a two-dimensional approximation of the wind at the crater floor:

$$\frac{du}{dt} + ku = -\frac{1}{\rho}\frac{\partial p}{\partial x}, \qquad (3)$$

where t is time, k is the friction coefficient, ρ is air density, and x is the east–west coordinate. The response time $1/k$ gives the time it takes for the wind at the crater floor to react to changes in forcing (i.e., to a change of the pressure gradient). Assuming stationary conditions, which is reasonable considering the immediate response of the wind component to the changes in the pressure difference (Fig. 9) and homogeneous conditions at the crater floor, which seems reasonable in the center, away from the sidewalls, (3) is reduced to a balance between the friction and pressure gradient forces. This simple balance reflects the linear relation between pressure difference and wind at the crater floor, which we have seen in Fig. 7. Further using the hydrostatic equation to express the pressure gradient through a temperature gradient yields

$$ku(z) = -\frac{1}{\rho}\frac{\partial p}{\partial x} = gT\int_z^{z_0}\frac{1}{T^2}\frac{\partial T}{\partial x}\,dz, \qquad (4)$$

where z_0 is the height where the temperature difference becomes 0 (i.e., at rim level). From the above equation we can calculate a response time $1/k$ based on typical values of u and Δp or ΔT (see section 4). Using $u = 1$ m s^{-1}, $\Delta p = 5$ Pa, and $\Delta x = 700$ m (or equivalently $u = 1$ m s^{-1}, $g = 10$ m s^{-2}, $T = 290$ K, $\Delta T = 1$ K, $\Delta x = 700$ m, and $\Delta z = 170$ m), (4) yields $1/k = 140$ s (or $1/k \approx 120$ s). Hennemuth (1986) derived a similar response time of 4 min for the cross-valley winds in the Dischma

Valley and 30 min for the along-valley winds. Vergeiner and Dreiseitl (1987) and Vergeiner et al. (1987) found $1/k = 45$ and 8 min, respectively, for the along-valley winds in the Inn Valley, Austria, and the Brush Creek Valley, Colorado. Considering the 5-min resolution of the data, a response time of about 2 min implies that we do not expect to see a lag between the pressure difference and the east–west wind component, which agrees with our findings from Fig. 9.

b. Relation between individual parameters

Filtered data indicate a linear relationship between cross-basin pressure differences and east–west wind components at the crater floor (Fig. 7), which is expressed by (4) as a balance between friction and pressure gradient forces. Data, however, indicate that the slope of the line formed by the medians is not constant over the entire pressure difference range, which implies that the friction coefficient k in (4) changes. Figure 7 suggests the distinction between two areas of different k: first, $(\Delta p)_{\mathrm{EW}} < -0.02$ hPa corresponding to the evening $(\Delta p)_{\mathrm{EW}}$ minimum with a larger friction coefficient, and, second, $(\Delta p)_{\mathrm{EW}} > -0.02$ hPa corresponding to the morning $(\Delta p)_{\mathrm{EW}}$ maximum and the afternoon period with a smaller friction coefficient. The afternoon period between the morning and evening maxima is characterized by weak wind speeds, which agrees with the smaller friction coefficient. The small number of data points contained in the individual categories of large absolute $(\Delta p)_{\mathrm{EW}}$, however, makes it difficult to fully interpret this transition.

Cross-basin temperature and pressure differences exhibit a nonlinear relation, particularly for stronger horizontal pressure gradients with magnitudes of $(\Delta p)_{\mathrm{EW}} > 0.03$ hPa (Fig. 6). Since $(\Delta p)_{\mathrm{EW}}$ at the crater floor is determined by the temperature gradients in the entire vertical column of the crater atmosphere, assuming that it is completely thermally driven and the pressure and temperature above the crater are horizontally homogeneous, we do not necessarily expect a linear relation [Eq. (4)]. A possible error source, however, exists in $(\Delta p)_{\mathrm{EW}}$ due to the simple correction of the vertical component of $(\Delta p)_{\mathrm{EW}}$ that is caused by the height difference between the west and east measurement sites. But the approximately linear relation between $(\Delta p)_{\mathrm{EW}}$ and u suggests that the correction filters out the vertical pressure gradient effectively. In this paper we look only at thermal effects. The weaker correlation between temperature and pressure differences may therefore also indicate additional contributions from nonthermal effects. Furthermore, the pressure difference may also be more exposed to influences from above the crater than other parameters, because the local pressure difference is determined by the entire vertical air column.

8. Conclusions

Data from the METCRAX field campaign in Arizona's Meteor Crater were analyzed with respect to the evolution of cross-basin winds during daytime. The analysis focused on quiescent days, when the wind field inside the crater basin was undisturbed and therefore determined mainly by thermal forcing. Horizontal wind components at the crater floor averaged over a 1-month period revealed a pronounced diurnal cycle. Wind direction changed from east or southeast in the morning, over south around noon, to west or southwest in the evening. The analysis of this daily change in wind direction along with an analysis of the difference in slope-parallel global radiation, the temperature difference, and the pressure difference between opposing sidewalls allowed us to determine that differential thermal heating is the main driving mechanism for the cross-basin flows under undisturbed and quiescent conditions. Good relationships between the individual parameters suggest that the asymmetric insolation causes a horizontal temperature gradient, which again causes a pressure gradient that finally produces the cross-basin flows at the crater floor.

Clearly, the small closed basin of the Meteor Crater facilitates observations of thermally driven cross-basin flows, which are undisturbed by larger-scale along-valley winds that occur in open valleys. The circular shape of the basin allows for the development of cross-basin temperature gradients throughout the day, with changing orientation as the sun moves across the sky. Due to the small horizontal dimensions of the crater the differential heating of the sidewalls produces a horizontal pressure gradient that is strong enough to produce observable wind speeds. The impacts of basin size on the evolution of cross-basin flows will be the focus of future work.

Acknowledgments. This material is based upon work supported by the National Science Foundation (NSF) under Grant ATM-0837870. Any opinions, findings, and conclusions or recommendations expressed in this material are those of the authors and do not necessarily reflect the views of NSF. Author ML received support from a DOC-fFORTE fellowship from the Austrian Academy of Sciences and from two scholarships from the University of Innsbruck (Doktoratsstipendium aus der Nachwuchsförderung der Leopold-Franzens Universität Innsbruck, and Stipendium für kurzfristige wissenschaftliche Arbeiten im Ausland). SWH received support from Army Research Office Grant 52734-EV. We thank the Barringer Crater Company and Meteor Crater Enterprises, Inc., for access to the field sites. The National Center for Atmospheric Research's Earth Observing Laboratory provided equipment, field support, and

quality-controlled datasets. We thank the staff of the NCAR Integrated Soundings System and Integrated Surface Flux System for their field and data processing assistance. We also thank two anonymous reviewers for their helpful comments on this manuscript.

APPENDIX

Correction of Temperatures from Nonaspirated Temperature Sensors

Overheating of the unaspirated temperature dataloggers and the unaspirated 0.5-m temperature sensor at the east upper tower occurred during daytime, even though the sensors were deployed in a radiation shield. Especially in the morning and evening when only one sidewall was sunlit, the radiation error led to an apparent intensified cross-basin temperature difference. Side-by-side comparisons of temperature dataloggers and aspirated temperature sensors at three sites in the crater were used to determine the coefficients in the following empirical function that was then used to correct for the radiation error:

$$T_{\text{corr}} = T - (c_1 - c_2 V) R_{\text{dir-N}}, \qquad \text{(A1)}$$

where T_{corr} is corrected temperature, T is observed temperature, V is wind speed (m s^{-1}) at 8.5 m AGL at the crater floor, and $R_{\text{dir-N}}$ is the direct normal radiation (W m^{-2}) at each logger location determined by multiplying $R_{\text{dir-N}}$ at the crater rim by a time-dependent factor (0 or 1) indicating shadowing or insolation of each site. At the rim, $R_{\text{dir-N}}$ was calculated by subtracting the measured diffuse from the measured global radiation and dividing by the cosine of the zenith angle. The direct normal component was used because the radiation shield is approximately spherical. Equation (A1) corrects the overheating that increases linearly with solar loading. Passive ventilation, which increases with wind speed, decreases the overheating. The analysis of data from the three collocated sensor pairs resulted in values of $c_1 = 0.001\ 86$°C (W m^{-2})$^{-1}$ and $c_2 = 0.000\ 25$°C (W m^{-1} s^{-1})$^{-1}$. This correction is applicable for wind speeds lower than $c_1/c_2 = 7.44$ m s^{-1}. Above this threshold, the correction would introduce a spurious heating. The filtered 8.5-m wind speeds at the crater floor never exceeded this threshold within the 30-day period. The correction of the radiation error reduced the mean offset between the temperature dataloggers and aspirated sensors from 1.30°C to a maximum of only 0.15°C. The standard deviation remained at 0.56°C. Since the radiation shield of the unaspirated 0.5-m temperature sensor at the east upper flux tower was identical to the shields of the temperature dataloggers, the same correction was applied to temperatures from this sensor.

REFERENCES

Anquetin, S., C. Guilbaud, and J.-P. Chollet, 1998: The formation and destruction of inversion layers within a deep valley. *J. Appl. Meteor.,* **37,** 1547–1560.

Bader, D. C., and C. D. Whiteman, 1989: Numerical simulation of cross-valley plume dispersion during the morning transition period. *J. Appl. Meteor.,* **28,** 652–664.

Colette, A., F. K. Chow, and R. L. Street, 2003: A numerical study of inversion-layer breakup and the effects of topographic shading in idealized valleys. *J. Appl. Meteor.,* **42,** 1255–1272.

Defant, F., 1949: Zur Theorie der Hangwinde, nebst Bemerkungen zur Theorie der Berg- und Talwinde. *Arch. Meteor. Geophys. Bioklimatol.,* **A1,** 421–450.

Egger, J., 1981: Thermally forced circulations in a valley. *Geophys. Astrophys. Fluid Dyn.,* **17,** 255–279.

Gleeson, T. A., 1951: On the theory of cross-valley winds arising from differential heating of the slopes. *J. Meteor.,* **8,** 398–405.

Gohm, A., and Coauthors, 2009: Air pollution transport in an Alpine valley: Results from airborne and ground-based observations. *Bound.-Layer Meteor.,* **131,** 441–463.

Gudiksen, P. H., and D. L. Shearer, 1989: The dispersion of atmospheric tracers in nocturnal drainage flows. *J. Appl. Meteor.,* **28,** 602–608.

Hennemuth, B., 1986: Thermal asymmetries and cross-valley circulation in a small Alpine valley. *Bound.-Layer Meteor.,* **36,** 371–394.

——, and H. Schmidt, 1985: Wind phenomena in the Dischma Valley during DISKUS. *Arch. Meteor. Geophys. Bioklimatol.,* **B35,** 361–387.

Hoch, S. W., and C. D. Whiteman, 2010: Topographic effects on the surface radiation balance in and around Arizona's Meteor Crater. *J. Appl. Meteor. Climatol.,* **49,** 1114–1128.

Kring, D. A., 2007: *Guidebook to the Geology of Barringer Meteorite Crater, Arizona (aka Meteor Crater): Fieldguide for the 70th Annual Meeting of the Meteoritical Society*. LPI Contribution 1355, Lunar and Planetary Institute, Houston, TX, 150 pp.

Lehner, M., and A. Gohm, 2010: Idealised simulations of daytime pollution transport in a steep valley and its sensitivity to thermal stratification and surface albedo. *Bound.-Layer Meteor.,* **134,** 327–351.

MacHattie, L. B., 1968: Kananaskis valley winds in summer. *J. Appl. Meteor.,* **7,** 348–352.

Matzinger, N., M. Andretta, E. van Gorsel, R. Vogt, A. Ohmura, and M. W. Rotach, 2003: Surface radiation budget in an Alpine valley. *Quart. J. Roy. Meteor. Soc.,* **129,** 877–895.

Moll, E., 1935: Aerologische Untersuchung periodischer Gebirgswinde in V-förmigen Alpentälern. *Beitr. Phys. Atmos.,* **22,** 177–199.

Orgill, M. M., 1989: Early morning ventilation of a gaseous tracer from a mountain valley. *J. Appl. Meteor.,* **28,** 636–651.

Segal, M., Y. Ookouchi, and R. A. Pielke, 1987: On the effect of steep slope orientation on the intensity of daytime upslope flow. *J. Atmos. Sci.,* **44,** 3587–3592.

Urfer-Henneberger, C., 1970: Neuere Beobachtungen über die Entwicklung des Schönwetterwindsystems in einem

V-förmigen Alpental (Dischmatal bei Davos). *Arch. Meteor. Geophys. Bioklimatol.,* **B18,** 21–42.

Vergeiner, I., and E. Dreiseitl, 1987: Valley winds and slope winds—Observations and elementary thoughts. *Meteor. Atmos. Phys.,* **36,** 264–286.

——, ——, and C. D. Whiteman, 1987: Dynamics of katabatic winds in Colorado's Brush Creek valley. *J. Atmos. Sci.,* **44,** 148–157.

Whiteman, C. D., 1989: Morning transition tracer experiments in a deep narrow valley. *J. Appl. Meteor.,* **28,** 626–635.

——, K. J. Allwine, L. J. Fritschen, M. M. Orgill, and J. R. Simpson, 1989: Deep valley radiation and surface energy budget microclimates. Part II: Energy budget. *J. Appl. Meteor.,* **28,** 427–437.

——, and Coauthors, 2008: METCRAX 2006—Meteorological experiments in Arizona's Meteor Crater. *Bull. Amer. Meteor. Soc.,* **89,** 1665–1680.

——, S. W. Hoch, M. Lehner, and T. Haiden, 2010: Nocturnal cold air intrusions into a closed basin: Observational evidence and conceptual model. *J. Appl. Meteor. Climatol.,* **49,** 1894–1905.